# Complex Precipitation Behavior in a Co-free High Entropy Alloy during Aging

Matthew Luebbe[1], Fan Zhang[2], Jonathan D. Poplawsky[3], Jiaqi Duan[1,4], Haiming Wen[1,*]

[1]Department of Materials Science and Engineering, Missouri University of Science and Technology, Rolla, MO 65409, USA

[2]Materials Measurement Science Division, National Institute of Science and Technology, Gaithersburg, MD 20899, USA

[3]Center for Nanophase Materials Sciences, Oak Ridge National Laboratory, TN 37996, USA

[4]Warwick Manufacturing Group, University of Warwick, Coventry, CV4 7AL, UK

*Corresponding author: wenha@mst.edu (H.M. Wen)

**Abstract**

High entropy alloys (HEAs) demonstrate high strength, thermal stability, and irradiation resistance, making them desirable for applications in nuclear reactors and other harsh environments. Many existing HEAs contain cobalt (Co), which makes them unsuitable for nuclear applications due to the long-term activation of Co. A previously studied Co-free alloy, $(Fe_{0.3}Ni_{0.3}Mn_{0.3}Cr_{0.1})_{88}Ti_4Al_8$, exhibits high strength but compromised ductility due to its network of brittle precipitates upon aging. This work investigates the formation mechanism and evolution of the precipitates, including $L1_2$ ($Ni_3Ti$ type, ordered face-centered cubic structure), B2 (NiAl type, ordered body-centered cubic structure), and Chi (FeCr-rich ordered α-Mn structure), in this alloy at 650 °C, the aging temperature that yields the alloy's peak strength after 120 hours. Using ex-situ scanning electron microscopy, transmission electron microscopy, and atom probe tomography, the precipitates were characterized in terms of their composition, morphology, and crystal structure at various aging times. In addition, synchrotron-based, in-situ X-ray diffraction was used to probe the evolution of precipitates in the bulk during key phases of in-situ aging. The $L1_2$ precipitates exhibit complex growth and coarsening behavior – their coarsening starts after just 24 hours, and competition between the $L1_2$ and B2 phases arises after 72 hours leading to a decrease in $L1_2$ volume fraction. Conversely, B2 and Chi precipitates exhibit delayed nucleation and growth, and do not form in observable quantities until after 24 hours. Once formed, however, these precipitates quickly dominate the microstructure, with >50% volume fraction after 120 hours, leading to the previously observed mechanical properties. This study provides a foundational understanding of the evolution of multi-precipitate structures in HEAs and guides future alloy development and optimization by tailoring the precipitates.

## 1. Introduction

High entropy alloys (HEAs) are a new and intriguing class of alloys with multiple principal elements. The typical definition of HEA is five or more elements with concentrations of 5-35 at% each [1-3]. This compositional complexity leads to severe lattice distortion, sluggish diffusion

kinetics, and high mixing entropy [1, 4]. Existing literature shows that HEAs possess unique properties, such as high strength and good ductility [5-9], good thermal and irradiation stability [10], and excellent oxidation resistance [11-12]. Although most studies have focused on single-phase structures, many recent studies have explored precipitation strengthening and intermetallic formation in HEAs [13-20]. For example, He et al [21] fabricated an $(FeCoNiCr)_{94}Ti_2Al_4$ alloy with a strength of 1100 MPa and a ductility of 40% by inducing $L1_2$ precipitation in a face-centered cubic (FCC) matrix with a combination of cold-rolling and aging. The $L1_2$ precipitates are ~20 nm diameter spherical particles evenly distributed in the matrix. In addition, a Co-free alloy $Al_{0.5}Cr_{0.9}FeNi_{2.5}V_{0.2}$ has been shown to possess an FCC+$L1_2$ spinodal structure with 1900 MPa strength and 9% ductility, also manufactured by cold-rolling and aging [22, 23]; in this alloy, the $L1_2$ precipitates are ~20 nm thick semi-continuous lamellae. These two alloys show that even with the same matrix and precipitate phases and similar processing, the microstructures, hence the mechanical properties, can vary greatly.

The unique properties of HEAs, such as sluggish diffusion and lattice distortion, lead to unusual precipitation kinetics. Some alloys, such as the $(FeCoNiCr)_{94}Ti_2Al_4$ previously discussed, show typical $L1_2$ coarsening kinetics, though with a much slower coarsening rate than Ni superalloys [18, 24-25]. Some of these alloys, such as the $(FeCoNiCr)_{94}Ti_2Al_4$ [24, 26] or Ni-30Co-13Fe-15CR-6Al-6Ti-0.1B [25], can form the $L2_1$, or Heusler phase, given enough time or a sufficient aging temperature. Therefore, understanding the kinetics involved is crucial to prevent the formation of this undesirable phase.

Often, given the large supersaturations of alloying elements, nucleation, growth and coarsening overlap [27, 28]. Other phases commonly studied, such as B2 and σ, can also be affected by the unusual thermodynamics and kinetics in HEAs [29-35]. For example, the nucleation and growth of σ phase in $Cr_{26}Mn_{20}Fe_{20}Co_{20}Ni_{14}$ matched the Johnson-Mehl-Avrami-Kolmogorov (JMAK) model almost perfectly, but their diffusion and coarsening kinetics were more complex [31-32]. Adding Al and Ti in different ratios to $Co_{1.5}CrFeNi_{1.5}$ HEA can produce needle-shaped B2, cuboidal γ', and cellular η [33]. While B2 and γ' fit a power law coarsening model, η consumes γ' to coarsen and its kinetics does not fit a normal coarsening model. These studies also show that different ratios of Ti and Al addition can result in other undesirable phases, such as B2 or η, in systems that were intended to be purely $L1_2$ strengthened [36-39].

In addition to the complexity induced by the nature of HEAs, systems with multiple precipitates can have complex precipitation mechanisms and pathways, such as competitive precipitation. Zhang et al [40] studied the simultaneous formation of $L1_2$ and $L2_1$ in an FeCoCrNiTiAl alloy system and observed that the phases competed for the Al in the alloy. With Ni content held constant at 30% or 35%, $L1_2$ was preferred over $L2_1$ with increasing Al content, but this trend was reversed with 25% Ni. Gwalani et al [41] showed a similar competition between $L1_2$ and B2 in an $Al_{0.3}CoCrFeNi$ system. For more traditional alloys, this phenomenon has been modeled [27, 42-44]. For example, competition between θ and γ' in Ni-Al-V alloys was studied with phase field kinetic models [42], and competition between different carbides in steels was predicted using diffusion models [43]. The kinetics of the competing phases interact with each other, making traditional single-phase kinetic models like JMAK invalid, but typically one phase

is kinetically favored, and the other thermodynamically favored [27]. The kinetically favored phase is only a metastable phase to be replaced by the thermodynamically favored phase over time. In addition, there can often be competition between continuous and discontinuous forms of the same precipitate phase. For example, Fang et al [45] indicated a competition between continuous and discontinuous (or homogeneously and heterogeneously nucleated) forms of $L1_2$ precipitation. Whether homogeneous or heterogeneous precipitation is favored depends on the system diffusion, the predicted phases, the heat-treatment temperature and the pre-existing strain and microstructure [46-48].

Our previous work [49] showed an unusual precipitate microstructure in the $(Fe_{0.3}Ni_{0.3}Mn_{0.3}Cr_{0.1})_{88}Ti_4Al_8$ alloy. This alloy exhibited nanoscale $L1_2$ in the FCC region and a network of B2 and Chi intermetallics after aging at 650 °C for 120 hours. This microstructure led to high strength but low ductility, with the low ductility most likely originating from the intermetallic network. Further development of this Co-free alloy requires mitigation of the network formation of these intermetallics, demanding a comprehensive understanding of the precipitation microstructure and its evolution. To meet this need, we explore the evolution of the precipitates in this alloy at 650 °C. The precipitation kinetics will be modeled and the unusual precipitation behavior will be explained based on thermodynamics. Using this knowledge, new alloys and aging treatments can be designed to avoid harmful precipitates and encourage the $L1_2$ precipitates.

## 2. Experimental Procedures

Bulk $(Fe_{0.3}Ni_{0.3}Mn_{0.3}Cr_{0.1})_{88}Ti_4Al_8$ was fabricated via vacuum induction melting of 99.9% pure elements. To ensure compositional homogeneity and a single-phase FCC structure, the cast was homogenized at 1100 °C for 48 hours, using carbon filled stainless steel bags to prevent oxidation. The homogenized sample was sectioned and aged at 650 °C for 0.5 to 244 hours. The samples were mechanically polished to a final step of 0.02 μm colloidal silica for characterization

Characterization of samples from various aging times was performed using scanning electron microscopy (SEM), electron backscatter diffraction (EBSD), transmission electron microscopy (TEM), and atom probe tomography (APT). SEM and EBSD were performed using a Helios Dual-Beam Nanolab SEM operating at 30 kV. TEM samples were prepared using focused ion beam (FIB) lift-out on the Helios and TEM characterization was performed using an FEI F20 TEM operating at 200 kV. Additional TEM was also performed on a JEOL JEM 2100F operating at 200 kV. The FIB on the Helios SEM was also used to prepare APT tips as described by Thompson *et al.* [50]. APT experiments were performed using a CAMECA local electrode atom probe (LEAP 4000XHR) in laser mode with a 30K sample base temperature and a 50 pJ laser energy. Reconstructions were created and analyzed with CAMECA's IVAS 3.8 software.

The evolution of precipitates phases during aging was also characterized using synchrotron-based X-ray diffraction measurements in the transmission mode. The measurements were conducted at the ultra-small-angle scattering facility of the Advanced Photon Source, Argonne National Laboratory [51]. 21 keV X-rays were used, with a photon flux density of $\sim 10^{13}$ photon/mm$^2$/s. The samples were ~80 μm in thickness to ensure X-ray transmission. A Pilatus 300 KW single photon counting device was used to collect the XRD data. A combined 30 s acquisition

time and the usage of Pilatus detector ensure that the weak diffraction signal from secondary phases is captured. A Linkam 1500 in-situ heating stage was used to age the sample and induce precipitation, while the precipitate evolution during the aging treatment was monitored by the X-ray diffraction. The heating rate was 150 °C/min, and the aging temperature was 650 °C with a holding time of 8 hours. More details about this type of measurements can be found elsewhere [52].

Chemical potentials of the elements and phases in thermodynamic equilibrium were calculated using Thermo-Calc, using the Ni 12.1 database. Hardness testing was performed using a Struers Duramin 5 Vickers hardness tester by applying a load of 4.91 N for a duration of 10 s. 10 data points were measured and averaged for hardness of each aging condition. Samples for SEM, EBSD, and hardness testing were mechanically polished with a final step of 0.02 μm colloidal silica.

## 3. Results

### *3.1 $L1_2$ precipitate evolution*

The primary precipitates that form in $(Fe_{0.3}Ni_{0.3}Mn_{0.3}Cr_{0.1})_{88}Ti_4Al_8$ based on previous work [49] are nanoscale $L1_2$ ($Ni_3Ti$ type, ordered FCC structure), microscale B2 (NiAl type, ordered body-centered cubic structure), and Chi (FeCr-rich ordered α-Mn structure). The $L1_2$ precipitates provide a considerable strengthening contribution, especially at short aging times. Figure 1 shows the evolution of $L1_2$ precipitates as observed via APT as defined by a 40 at.% Ni isoconcentration surface. The values for size, volume fraction in FCC phase, and number density of the $L1_2$ precipitates as determined by APT are shown in Figure 2. The $L1_2$ precipitates start very small, about 5 ± 1 nm in diameter at 2 hours and grow to 14 ± 3 nm after 24 hours. Their sizes continue to increase throughout the aging; however, the increase is significantly slower later, with the average diameter reaching 22 ± 7 nm after 120 hours and 25 ± 8 nm after 244 hours of aging. Note the dramatic change in slope for all three values (Figure 2d-f) from 12 to 24 hours. At this point, the rate at which the volume fraction and size increase and the number density decreases all decline, with different trends after the time for the different metrics. The volume fraction also shows a drop from 48 hours to 72 hours, with a minimum of 21 ± 4% reached at 120 hours. After this minimum, the volume fraction of $L1_2$ in the FCC matrix returns to 30 ± 1% after 244 hours. These volume fraction results are consistent between both tips of each aging condition. This trend is due to the competition between $L1_2$ precipitation and B2 precipitation, which will be elaborated on further in the discussion section.

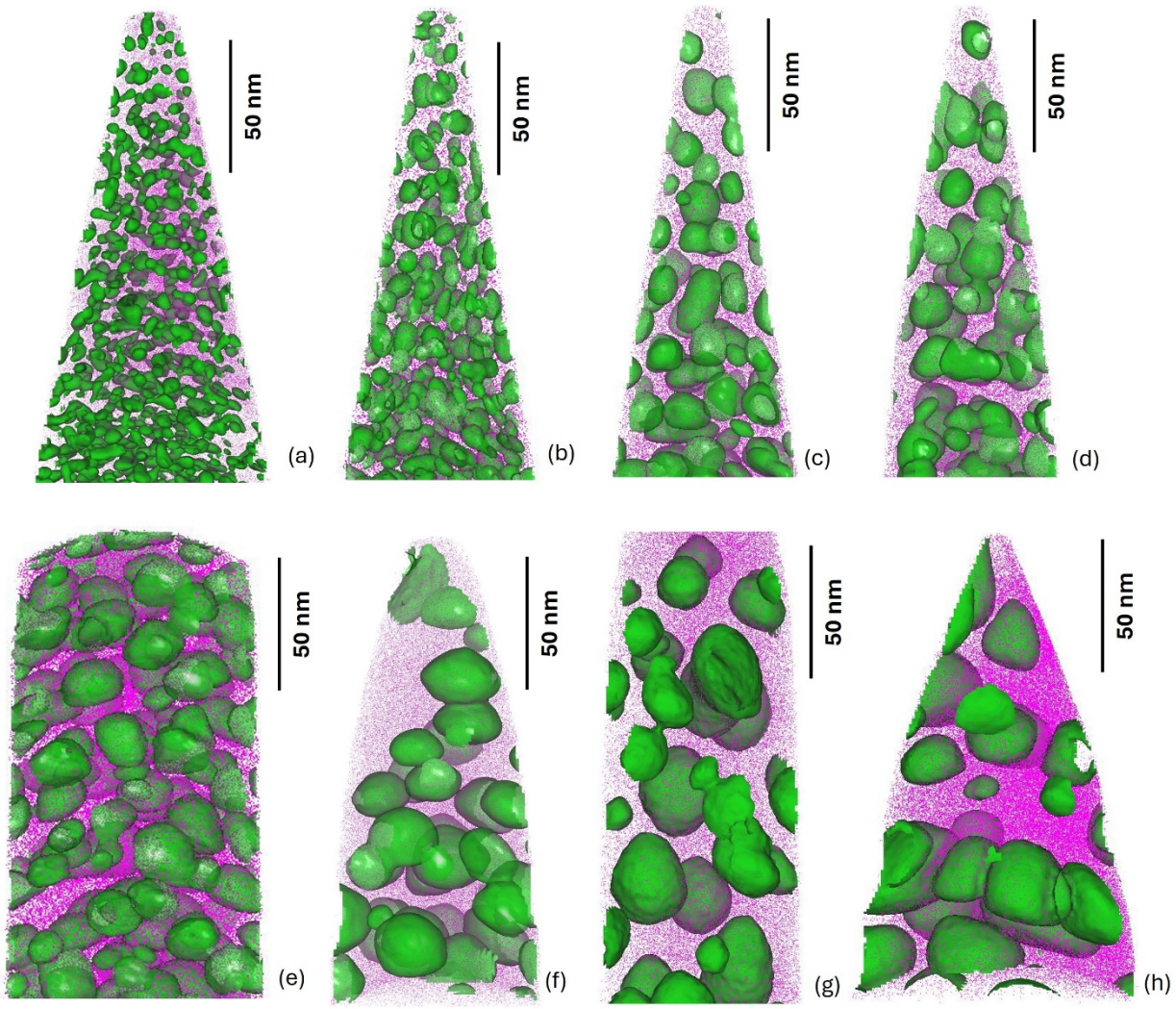


**Figure 1**: APT reconstructions from $(Fe_{0.3}Ni_{0.3}Mn_{0.3}Cr_{0.1})_{88}Ti_4Al_8$ aged at 650 °C for (a) 2 hours, (b) 6 hours, (c) 12 hours (d) 24 hours, (e) 48 hours, (f) 72 hours, (g) 120 hours, and (h) 244 hours. 40% Ni isosurface in each shows growth of L12 precipitates during aging.

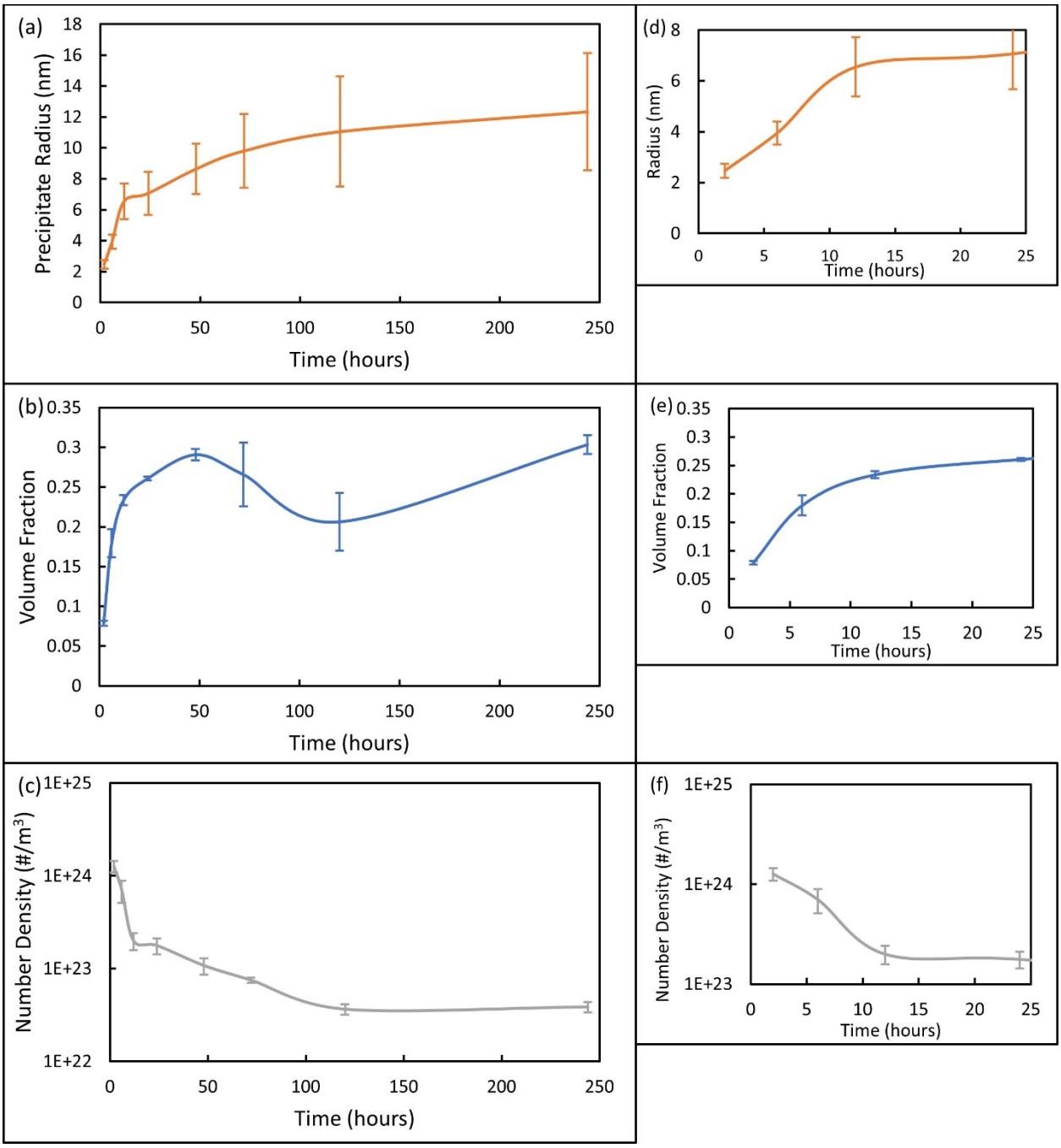


**Figure 2**: APT Analysis of L12 precipitate evolution in $(Fe_{0.3}Ni_{0.3}Mn_{0.3}Cr_{0.1})_{88}Ti_4Al_8$ under 650 °C aging showing change in (a,d) radius, (b,e) volume fraction, and (c,f) number density. Notice the abrupt change in growth at 12 hours, illustrated in (d-f). Volume fraction of $L1_2$ is in the FCC region, not the alloy as a whole.

*3.2 B2 and Chi evolution*

In addition to the $L1_2$ nanoprecipitates, $(Fe_{0.3}Ni_{0.3}Mn_{0.3}Cr_{0.1})_{88}Ti_4Al_8$ also exhibits a network of B2 and Chi phases. This network starts to form after 24 hours of aging and grows to

dominate the microstructure during the subsequent aging, as shown in the secondary electron SEM images in Figure 3. It can be seen in Figure 4d that B2 and Chi co-precipitate, with B2 initially dominating. These precipitates grow together to form the network observed at 120 hours and 244 hours, however, the formation of Chi occurs quickly. The network becomes increasingly occupied by the Chi phase from 120 to 244 hours, as Chi increases from 22.14% ± 5.39% to 24.52% ± 1.97%, while B2 falls from 28.95% ± 3.19% to 25.75% ± 3.11%.

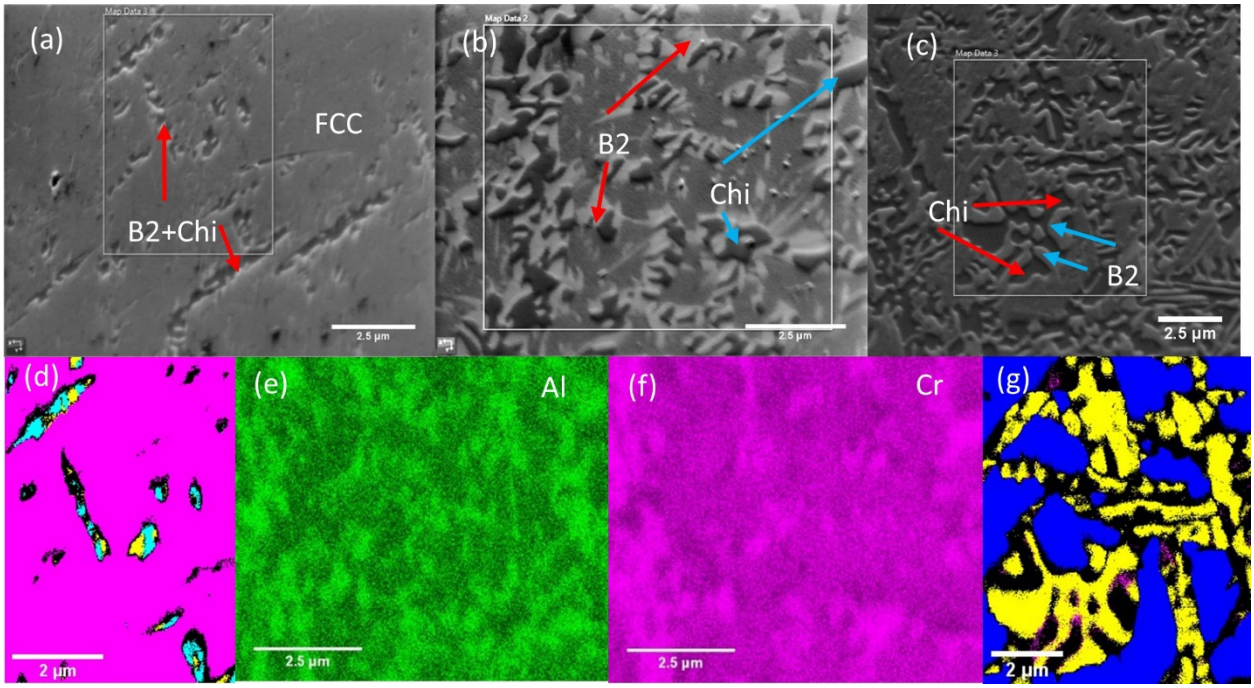


**Figure 3**: Secondary electron SEM images of $(Fe_{0.3}Ni_{0.3}Mn_{0.3}Cr_{0.1})_{88}Ti_4Al_8$ aged at 650 °C for (a) 24 hours, (b) 120 hours, and (c) 244 hours. Dark regions on all images are Chi, adjacent light regions are B2. (d) EBSD phase map after 24 hours aging, pink=FCC, blue=Chi, yellow=B2. B2+Chi form as distinct precipitates. (e), (f) Al and Cr EDS maps after 120 hours aging, showing Al-rich B2 and Cr-rich Chi. (g) EBSD phase map after 244 hours aging, blue=FCC, yellow=Chi, pink=B2. Chi increasingly occupies the network at longer aging times.

TEM images of the microstructure are shown in Figure 4. The B2 precipitate shows a lined structure, especially when it grows past a certain size. In addition, B2, unlike Chi, forms smaller isolated precipitates within the FCC matrix, as labeled in Figure 4a and 4b. This indicates that the B2 phase is the originator of the B2-Chi group, with Chi forming on existing B2. To further confirm this theory, STEM was taken of the B2 and Chi after 24 hour aging as shown in Figure 5. The B2 phase, otherwise isolated in the FCC matrix, shows Cr enrichment on its edges, which likely serves as a nucleation site for the Chi phase to form. This suggests that the B2 and Chi network is the result of chemical segregation around the B2 precipitates as they form and grow. In addition, the increasing prevalence of Chi in the structure as aging continues suggests that the Chi phase is more thermodynamically favorable than the B2 phase. This will be further elaborated in the discussion section.

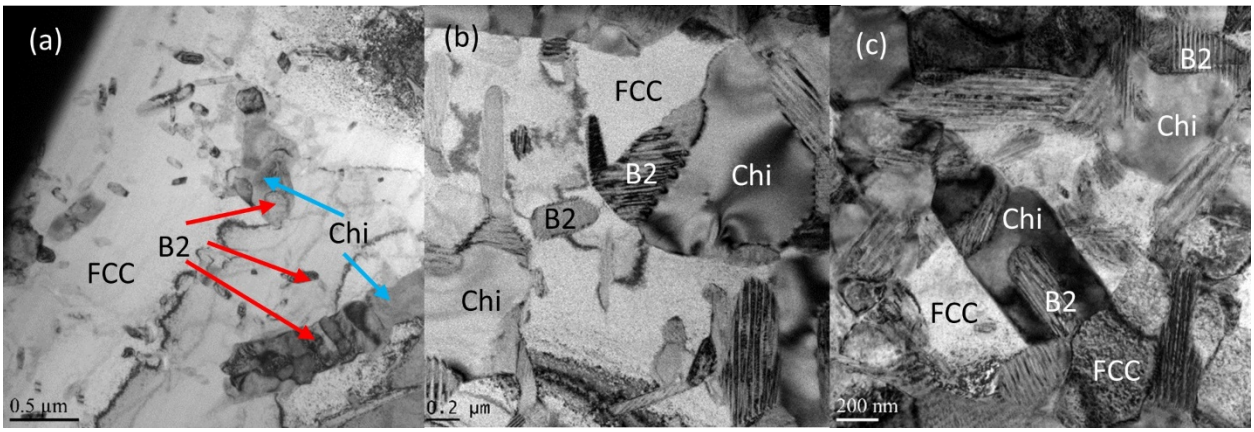


**Figure 4**: TEM images of $(Fe_{0.3}Ni_{0.3}Mn_{0.3}Cr_{0.1})_{88}Ti_4Al_8$ aged at 650 °C for (a) 24 hours, (b) 120 hours, and (c) 244 hours. Examples of each phase are labeled. The 24 hours samples show some large B2+Chi structures, but mostly consists of smaller (100 nm) B2. The 120 and 244 hours samples show larger B2 and Chi and less of the smaller B2, although it is still present. B2 phases can be easily identified through their lined structures under TEM.

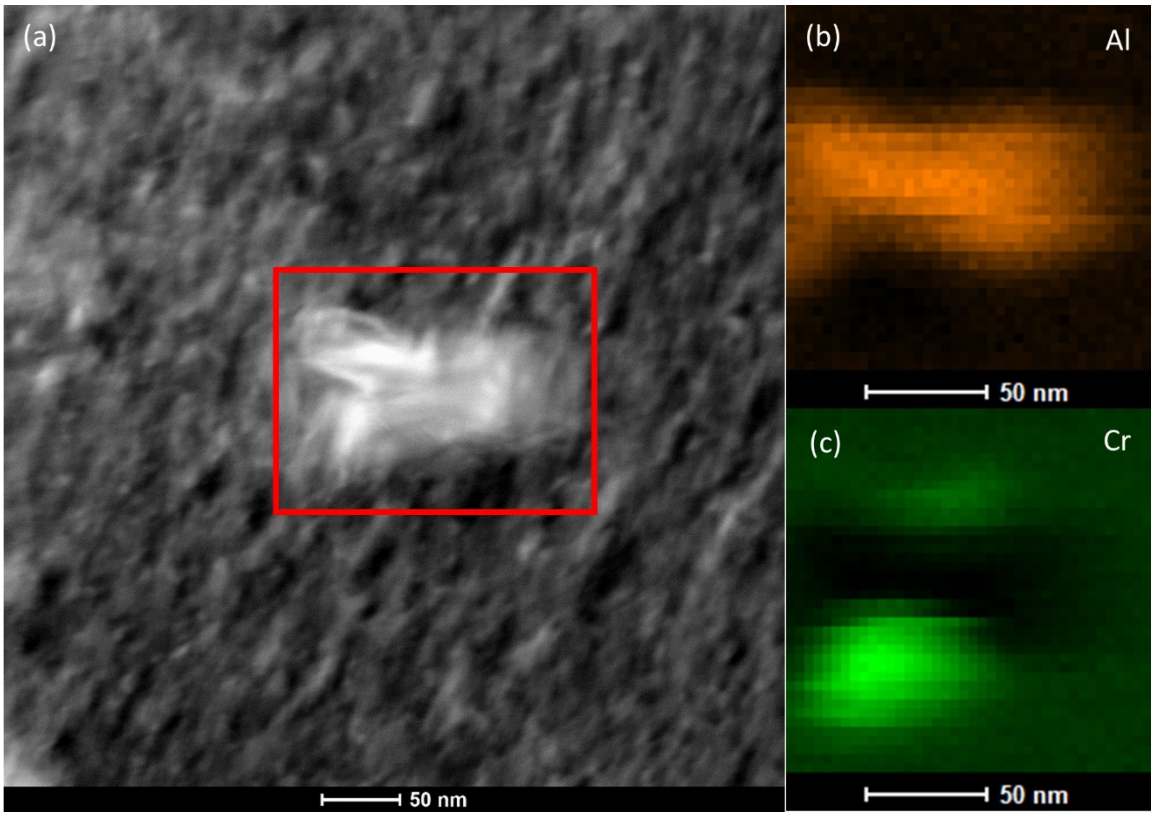


**Figure 5**: Scanning TEM (STEM) images of $(Fe_{0.3}Ni_{0.3}Mn_{0.3}Cr_{0.1})_{88}Ti_4Al_8$ aged at 650 °C for 24 hours. (a) Dark-field STEM image showing an isolated B2 precipitate, confirmed by (b) Al map. (c) Cr map showing enrichment at the edges of the B2, approaching 25 at%. This enrichment likely serves as a seed for forming Chi.

*3.3 Hardness evolution during aging*

The hardness evolution in $Fe_{0.3}Ni_{0.3}Mn_{0.3}Cr_{0.1})_{88}Ti_4Al_8$ during aging at 650 °C is shown in Figure 6. Aging leads to rapid hardening in the first 24 hours, followed by gradual rise to the peak hardness of 535 HV after 120 hours. Extending aging up to 244 hours exhibits marginal reduction in hardness. The different hardness regimes appear to match changes in the precipitation behavior, with the dramatic rise in hardness likely caused by the rapid growth of $L1_2$ precipitation, and the more gradual hardness increases caused by the growth of B2 and Chi after 24 hours.

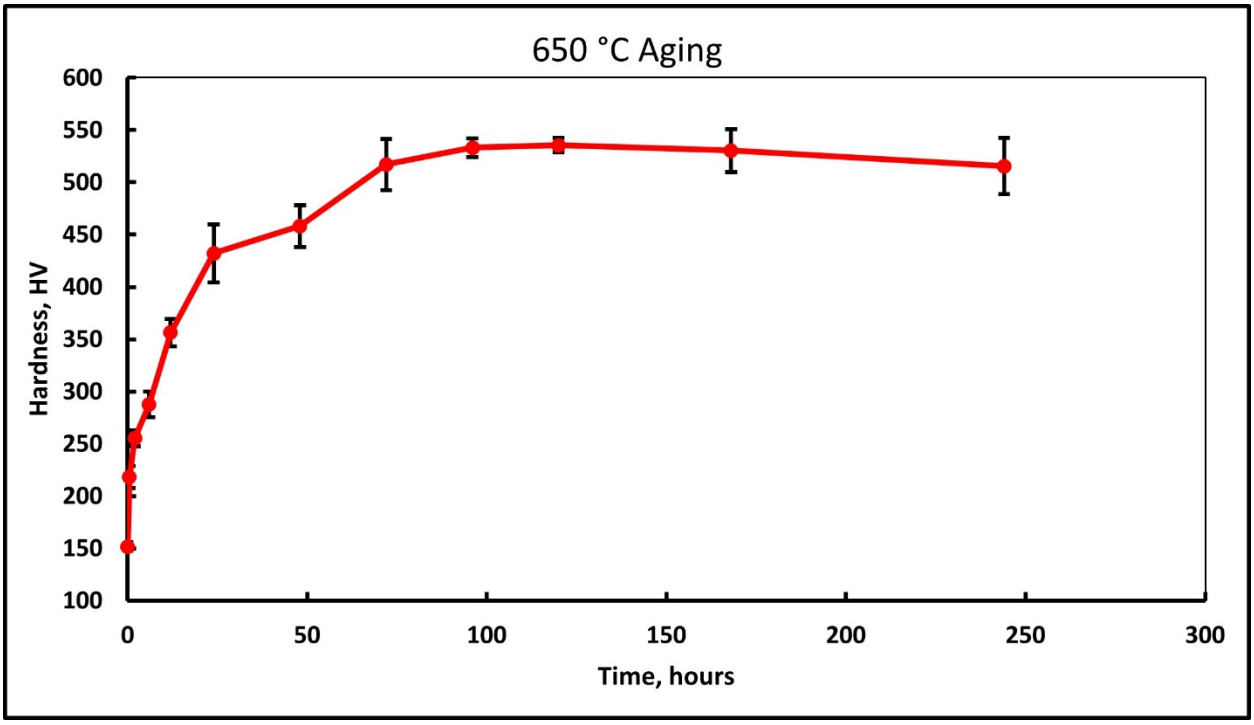


**Figure 6**: Vickers hardness of $(Fe_{0.3}Ni_{0.3}Mn_{0.3}Cr_{0.1})_{88}Ti_4Al_8$ aged at 650 °C for different times up to 244 hours. Hardness increases rapidly up to 24 hours aging, then slowly increases to a peak of 535 HV at 120 hours. Overaging causes little reduction in hardness.

*3.4 Phase evolution during in-situ aging revealed by XRD*

In-situ aging of $(Fe_{0.3}Ni_{0.3}Mn_{0.3}Cr_{0.1})_{88}Ti_4Al_8$ was performed with simultaneous XRD analysis to determine the precipitation kinetics at 650 °C aging. Aging was performed on both the homogenized sample, to highlight the early growth of $L1_2$ in Figure 7, and a sample pre-aged at 650 °C for 24 hours, to show the growth of B2 and Chi and the coarsening of $L1_2$ in Figure 8. Figure 7a displays the XRD patterns used for analysis, with major peaks from each phase labeled. By 200 minutes, only FCC and $L1_2$ have multiple visible peaks, with only the strongest B2 and Chi peaks visible, indicating that their volumes are small. More peaks appear as the phases continue to form. The volume fraction (Figures 7b, 8b) evolution trend was determined by the changes in integrated peak intensity to be discussed in Section 4.1, with the absolute numbers corrected to the known volume fraction from EBSD and APT. The number correction was necessary because the FCC matrix has very large grains (400 μm, larger than interaction volume)

and the Chi phase is highly textured, making quantitative results from XRD unreliable. The texture was determined based on the 2D XRD intensity map shown as a subset of Figure 7a, with the Chi peaks visible as individual spots as opposed to the rings for FCC matrix (and $L1_2$) showing that the Chi phase orientation is not random. In addition, average size (Figures 7c, 8c) is crystallite size, not precipitate size as observed from APT and EBSD, but the trend can also be assumed to be analogous for both. $L1_2$ shows consistent increases in both volume fraction (in FCC matrix) and size at early aging times. B2 and Chi do not form until after 3.3 hours of aging and show similar trends. Their volume fractions increase at a similar rate to each other, though at a noticeably slower rate than $L1_2$. Their sizes barely change during aging, suggesting that these precipitates are primarily nucleating at this stage. The noise in the B2 size curve in Figure 7c is due to the low intensity of the B2 peaks shown in Figure 7a, which makes peak width calculations unreliable. At early times, the average measurement error goes up due to these weak peaks as well, making any trends in size difficult to determine. After 24 hours of aging before in-situ aging, all three phases are well-established, and their further evolution is of interest. $L1_2$ slightly decreases in volume fraction and size, suggesting that the additional growth of B2 and Chi occurs at the expense of the $L1_2$ precipitates. B2 and Chi both grow slightly in size but Chi grows slightly more than B2 in volume fraction, suggesting that B2 may have reached the coarsening stage, while Chi is still growing. The average errors for Figure 8 and later times in Figure 7 are ~7% for volume fraction and ~5% for size.

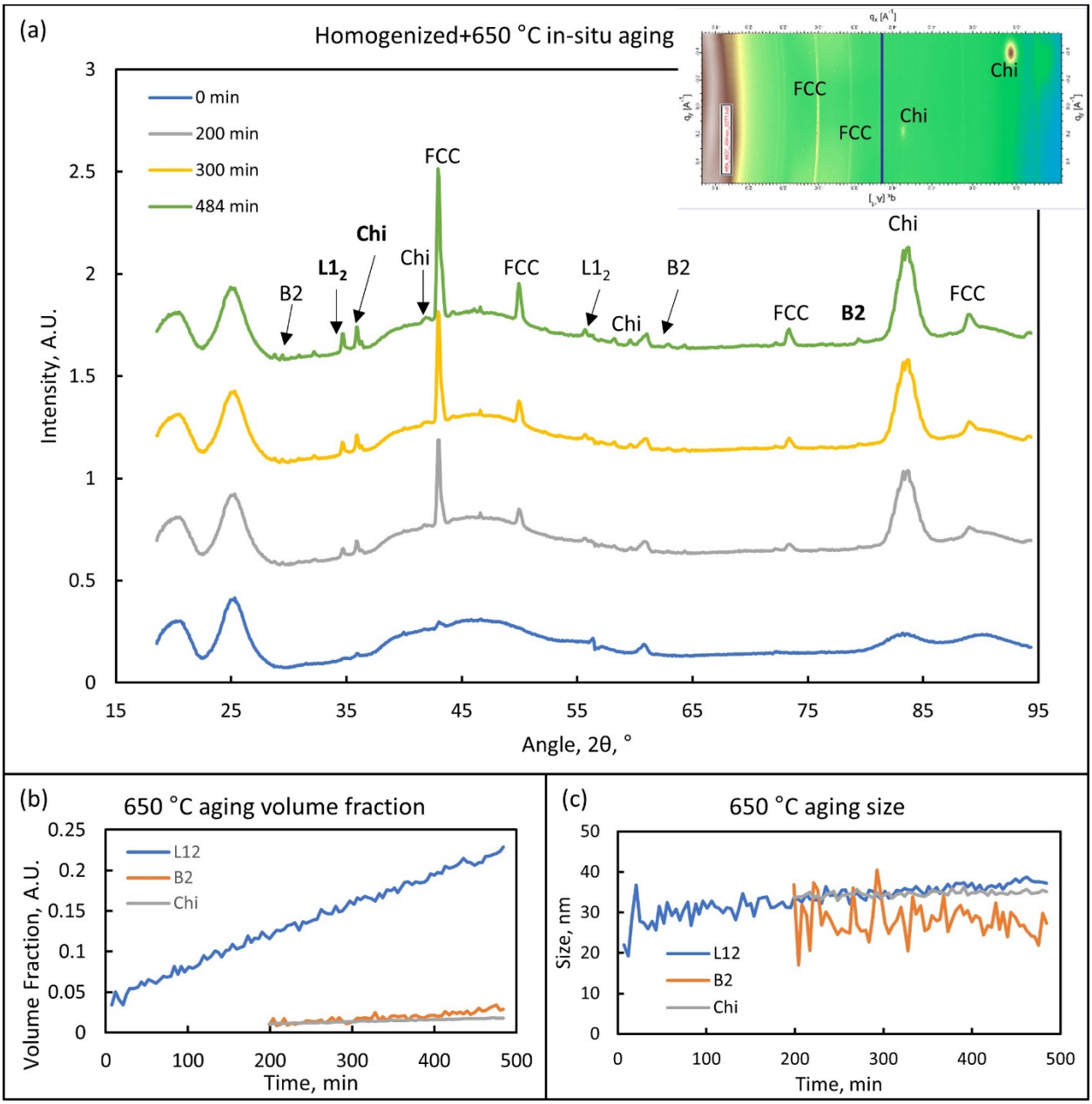


**Figure 7**: XRD analysis of $(Fe_{0.3}Ni_{0.3}Mn_{0.3}Cr_{0.1})_{88}Ti_4Al_8$ during in-situ aging at 650 °C, starting from the homogenized state: (a) XRD patterns of selected timesteps during the in-situ aging, with important peaks highlighted; the subset in (a) shows the 2D XRD plot for 484 min, with strong peaks labeled to show Chi phase texture(b) volume fraction of the three precipitate phases, using arbitrary units so trends are highlighted; (c) size of the three precipitate phases taken from Williamson-Hall analysis of bold labeled peaks in (a) assuming minimal strain.

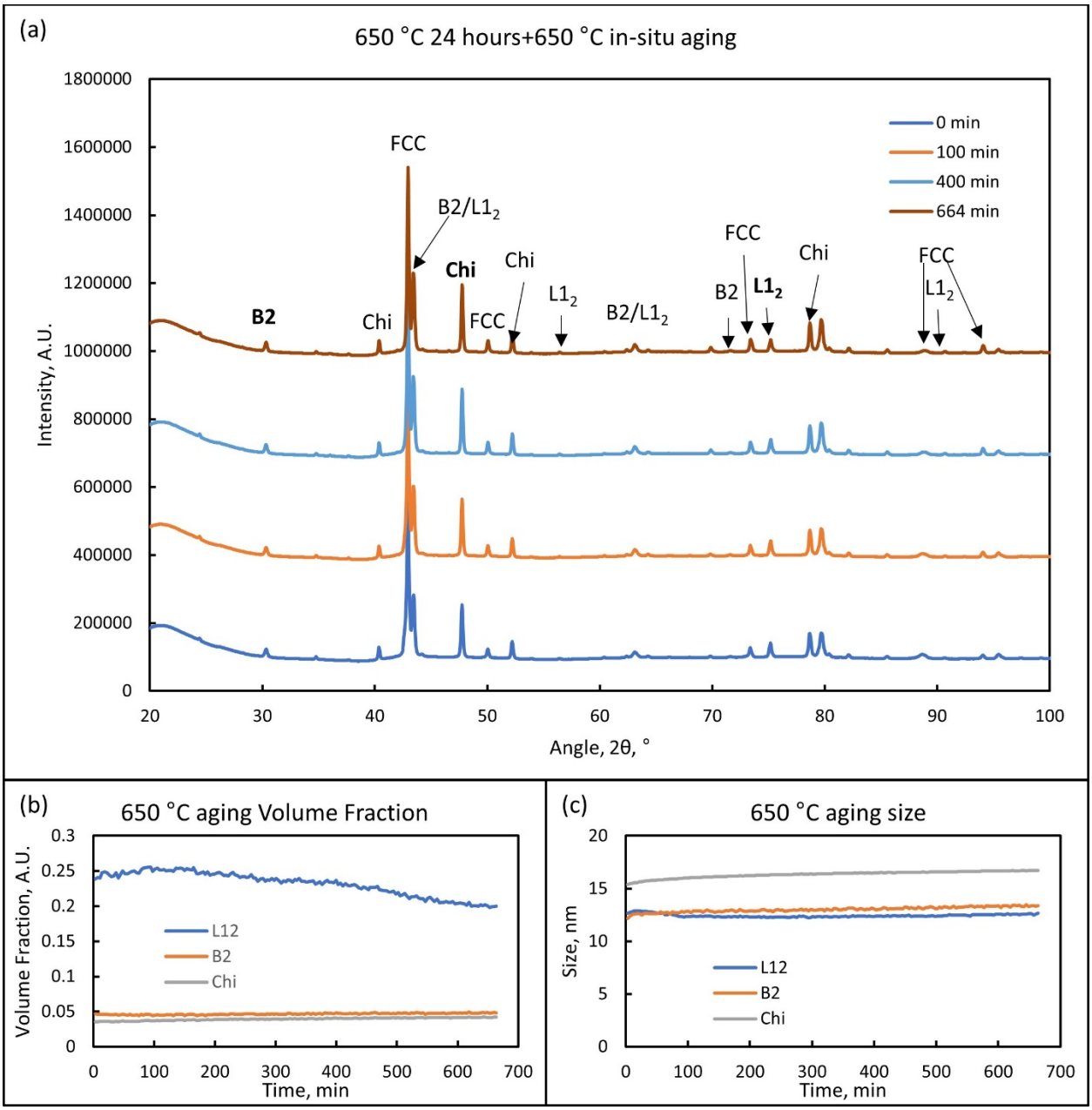


**Figure 8**: XRD analysis of $(Fe_{0.3}Ni_{0.3}Mn_{0.3}Cr_{0.1})_{88}Ti_4Al_8$ during in-situ aging at 650 °C, starting from the 650 °C 24 hours aged state: (a) XRD patterns of selected timesteps during the in-situ aging, with important peaks highlighted; (b) volume fraction of the three precipitate phases, using arbitrary units so trends are highlighted; (c) size of the three precipitate phases taken from Williamson-Hall analysis of bold labeled peaks in (a) assuming minimal strain.

## 4. Discussion

### *4.1 XRD Analysis*

Volume fraction was calculated from the integrated peak intensity using the following equation derived from the equation for peak intensity under XRD [53]:

$$\frac{I_{(hkl)j}}{I_{(hkl)i}} = \frac{M_{(hkl)j}V_i^2\left|F_{(hkl)j}\right|^2\left(\frac{1+cos^2(2\theta)cos^2(2\theta_m)}{sin^2 2\theta\cos\theta}\right)_{(hkl)j}}{M_{(hkl)i}V_j^2\left|F_{(hkl)i}\right|^2\left(\frac{1+cos^2(2\theta)cos^2(2\theta_m)}{sin^2 2\theta\cos\theta}\right)_{(hkl)i}}\frac{v_j}{v_i}$$

Where I is the integrated intensity, M is the multiplicity of the peak, V is the unit cell volume for the phase, F is the structure factor of the peak and phase, $\frac{1+cos^2(2\theta)cos^2(2\theta_m)}{sin^2 2\theta\cos\theta}$ is the Lorentz factor with $\theta_m$ being the monochromator diffraction angle, v is the volume fraction, and i and j refer to any two phases whose volume fractions are being compared. However, the XRD calculated volume fractions do not match the known volume fractions of phases as established by APT and EBSD due to the large FCC grains and the textured nature of the Chi phases, as determined based on the 2D XRD intensity maps. Nevertheless, the trend was still of interest and was examined in Figures 7b and 8b, with the exact numbers corrected based on known volume fractions determined from APT and EBSD. It is worth noting that the APT volume fraction has some error due to local magnification aberration, but the APT data is still useful as a comparison. The known volume fractions at 6 hours (B2 and Chi assumed to be 2 and 1.5%, respectively) and 24 hours were taken from Figure 2 and Table 1, and the volume fractions obtained from the XRD intensity equation were multiplied by a constant factor to get them to match the known values at the known times.

Crystallite size of the precipitate phases was estimated based on the peak broadening determined from XRD patterns using the Williamson-Hall equation:

$$\beta cos\theta = \frac{K\lambda}{D} + (4sin\theta)$$

Where β is the peak broadening, K=0.9, λ=0.5904 is the wavelength used in the synchrotron, D is the precipitate size, and ε is the lattice strain. Considering that the alloy was cast, homogenized, and aged, the lattice strain term is assumed to be negligible, so the equation reduces to the Scherrer equation:

$$\beta cos\theta = \frac{K\lambda}{D}$$

The XRD estimated crystallite sizes do not match the precipitate size measured from APT and EBSD because these methods measure different dimensions of precipitates (XRD: dimensions of coherent scattering domain; Precipitate size from APT or EBSD: physical dimensions of the secondary phase particles within a matrix). In principle, the precipitate size shall always be the same or greater than the crystallite size. In our case, the presence of internal defects is evident in the TEM data (Figure 5), rendering the coherent scattering domain size provided by the Scherrer equation consistently smaller than the physical precipitate size observed by APT and EBSD. Nevertheless, the trends for size change are still relevant to gain insight regarding the kinetics of precipitation.

*4.2 $L1_2$ precipitation kinetics*

To understand the precipitation kinetics, the Lifshitz-Slyozov-Wagner (LSW) coarsening model [27, 54, 55] was used to fit the precipitate size data from APT, with $r^3$ plotted versus t, assuming diffusive growth, graph shown in Figure 9. Although the traditional LSW model involves constant volume and pure coarsening, the apparent predominance of coarsening after 24 hours in the $L1_2$ precipitates and relatively minor changes in volume fraction from 24 to 120 hours renders the use of this model appropriate. [54, 55]. Nucleation and growth do not fit the LSW model, so these regions will not fit the line. The coarsening rate k appears to be relatively constant from 24-120 hours with a slight slope change at 72 hours, but severe deviations are observed before 24 hours and after 120 hours. Aging before 24 hours can be attributed to mixed nucleation, growth and coarsening, thus the deviation from linear behavior, but the deviation from LSW model for aging after 120 hours remains unexplained. Given the increase in volume fraction (Figure 2b) and slight increase in number density (Figure 2c) after 120 hours of aging, it is possible that a second round of nucleation occurs after long aging times. This is likely due to the dissolution of B2 at longer times leading to more Ni atoms released into the matrix, allowing additional $L1_2$ to form, likely homogeneously in the FCC matrix. The complex interplay between the $L1_2$ and B2 formations poses substantial obstacles to accurately modeling the precipitation kinetics of these phases. This becomes particularly challenging when the B2 phase becomes more volumetrically significant [27].

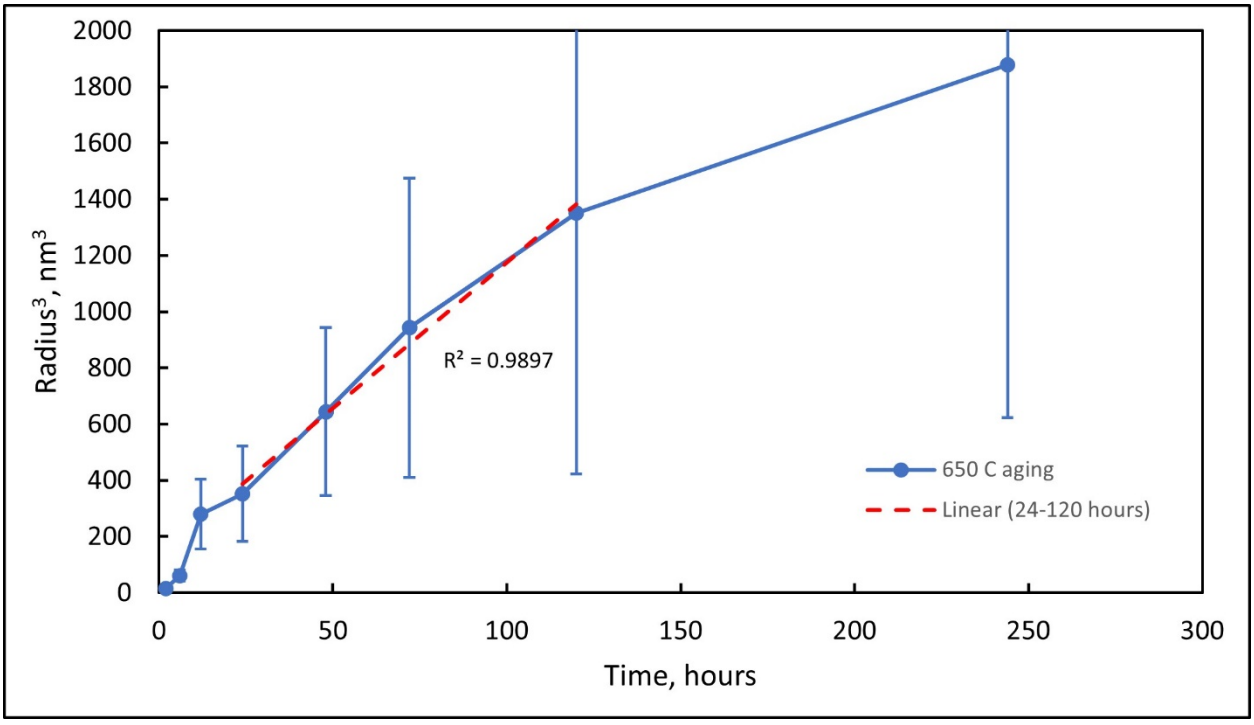


**Figure 9**: Fitting of $L1_2$ precipitate sizes from APT to the LSW coarsening model.

Additional explanations can be made for why the LSW model does not fit perfectly to the kinetics of the $L1_2$ precipitates beyond the interaction between B2 and $L1_2$. Specifically, in this alloy, nucleation, growth and coarsening cannot be separated. Robson's 2004 study [28] showed that the nucleation, growth, and coarsening can overlap given a low enough interfacial energy

between the precipitate and matrix, or a high enough supersaturation of alloying elements in the initial matrix. While the interfacial energy is not known exactly for this alloy, it can be assumed to be low considering the coherent interface between the FCC matrix and $L1_2$ precipitates. The supersaturation for both Al and Ti is high, as the alloy contains 8 at% and 4 at% of them respectively, while the equilibrium matrix composition after aging contains only ~1 at% of each based on APT results from our prior works [49]. This indicates that the alloy is in the regime where $L1_2$ would simultaneously nucleate, grow and coarsen for a significant amount of the aging time, which can explain the trends in Figure 2. This could also explain the continuous decrease of the number density of $L1_2$ shown in Figure 2c, which would be expected of coarsening, but not of growth.

*4.3 Thermodynamics and kinetics for B2 and Chi precipitation*

Table 1 gives precipitate statistics for B2 and Chi under 3 different aging conditions. Only limited data points were recorded for the precipitation of B2 and Chi, so no kinetics models were tried, but the kinetics will be discussed. The total volume fraction of B2 and Chi grow from less than 10% of the structure after 24 hours to over 50% of the structure after 120 hours, but do not grow further after that. However, the amount of the structure that is B2 or Chi changes constantly. B2 is continually the majority of the network but its size is always smaller than Chi in the network. In addition, the number density of B2 continually decreases while that of Chi continually increases. Figure 8c shows that B2 volume fraction remains constant while Chi volume fraction increases, suggesting that Chi precipitates continually nucleate and grow off B2 precipitates, while B2 precipitates continually coarsen and eventually disappear, if aging time is long enough, due to the growth of Chi precipitates. The precipitation process is shown schematically in Figure 10.

The reasons for why continuous Chi growth would cause B2 to decrease as well as why B2 growth causes $L1_2$ to dissolve, can be examined based on thermodynamics. $L1_2$ forms early due to fast precipitation kinetics, as $L1_2$ ($2.13\times10^{-19}$ J) has a lower nucleation barrier for formation in an FCC matrix than B2 ($4.23\times10^{-19}$ J) based on calculations from Thermo-Calc using the Ni 12.1 database. However, B2 is thermodynamically favorable over $L1_2$, as illustrated by Figure 11a-b illustrating Ni and Al's preference for B2 over $Ni_3Ti$, which is used as a stand-in for $L1_2$. As B2 grows, Chi grows along with it, consuming the Fe and Cr in the matrix until both phases reach saturation. However, once saturated, Chi is thermodynamically favorable over B2, as shown in Figure 11c-d, as the Ti and Mn, which are in relatively equal proportions in both B2 and Chi based on previous results [49], nevertheless have a chemical potential driving force to form Chi over B2. It is worth noting that Chi phase was not included by Thermo-Calc HEA 6.1 or Ni 12.1 databases, the latter of which was used for the calculations, so two stand-ins were used: Sigma, which is the equilibrium predicted phase as reported in our previous work [49], and α-Mn, which has the same structure as Chi. The preference especially of Ti for Chi over B2 causes Chi to grow at B2's expense, as shown in Table 1. This partial dissolution of B2 will introduce more Ni to the matrix, favoring $L1_2$ precipitation as shown by Liu et al [56]. This explains the increase in $L1_2$ volume fraction from 120 hours to 244 hours observed in Figure 2. This hypothesis is also supported by the histogram in Figure 10f, which shows an increase in small (0-5 nm) precipitates from 120 hours to 244 hours, indicating new precipitate nucleation.

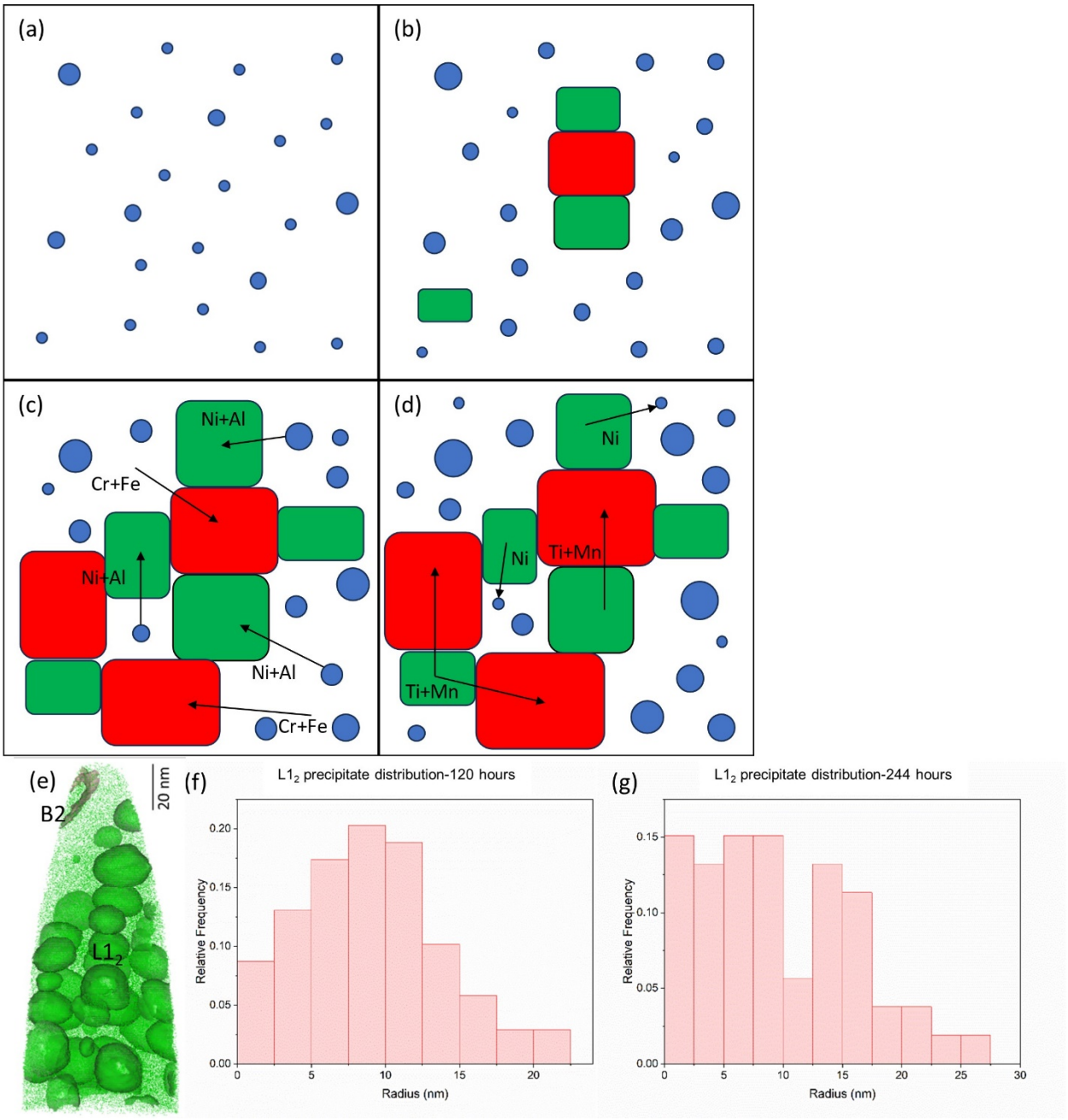


**Figure 10:** (a-d) Schematic of precipitation procedure in $(Fe_{0.3}Ni_{0.3}Mn_{0.3}Cr_{0.1})_{88}Ti_4Al_8$, with blue=$L1_2$, Green=B2, Red=Chi: (a) early aging (0-24 hours) with only $L1_2$ present; (b) 24-48 hours, B2 and Chi appear, $L1_2$ is coarsening; (c) late aging (72-120 hours) with B2 and Chi having grown and some $L1_2$ dissolving in favor of B2; and (d) overaging (244 hours) with Chi consuming B2, and the Ni from B2 forming new $L1_2$ precipitates. (e) APT reconstruction of 72 hours aged sample, with 40% Ni isosurface showing B2 and $L1_2$. Note the absence of $L1_2$ around B2. (f) and (g) Histograms of $L1_2$ precipitate sizes at 120 hours and 244 hours aging, respectively, determined from APT. Note the increase in small (0-2.5 nm) precipitates indicating nucleation of new precipitates.

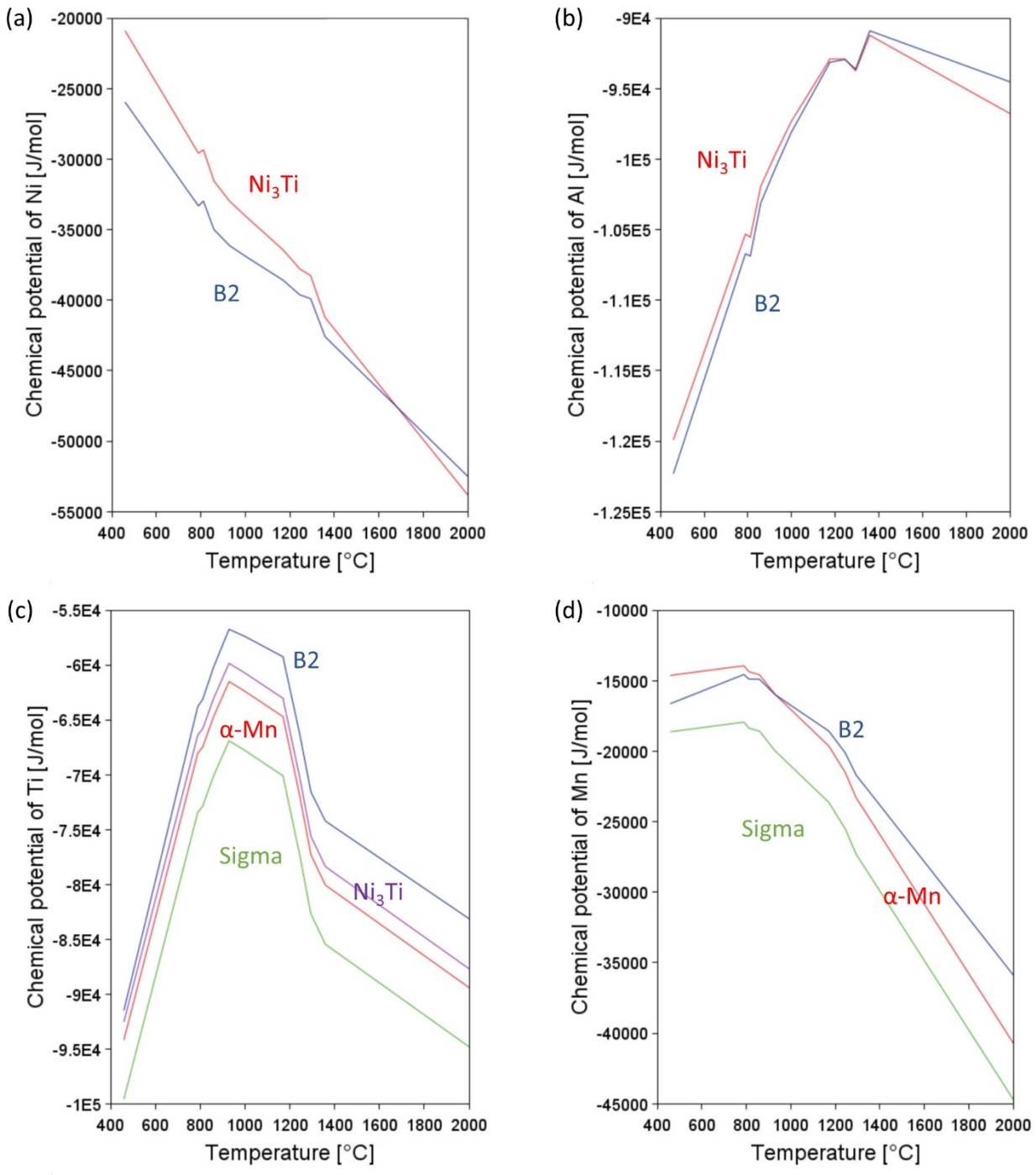


**Figure 11:** Chemical potential of selected elements and phases in $(Fe_{0.3}Ni_{0.3}Mn_{0.3}Cr_{0.1})_{88}Ti_4Al_8$ using the Thermo-Calc Ni 12 database: (a) Ni and (b) Al show a clear preference for B2 over $L1_2$ at lower temperatures, including 650 °C; (c) Ti shows a clear preference for sigma and α-Mn, two Chi stand-ins, over B2; (d) Mn shows a slight preference for sigma over B2, but not α-Mn over B2 at 650 °C.

**Table 1:** Precipitate statistics for B2 and Chi under 3 different aging conditions

| Aging Condition | Average Radius (nm) | Number Density ($/m^3$) | Area Fraction (%) |
|---|---|---|---|
| 650 °C 24 hours | | | |
| B2 | 172 ± 36 | 2.01 ± 0.64E12 | 4.67 ± 1.74 |
| Chi | 240 ± 93 | 7.84 ± 2.50E11 | 3.58 ± 1.33 |
| 650 °C 120 hours | | | |
| B2 | 330 ± 56 | 1.93 ± 0.66E12 | 28.95 ± 3.19 |
| Chi | 360 ± 72 | 1.14 ± 0.29E12 | 22.14 ± 5.39 |
| 650 °C 244 hours | | | |
| B2 | 434 ± 216 | 1.74 ± 0.18E12 | 25.75 ± 3.11 |
| Chi | 502 ± 96 | 1.24 ± 0.51E12 | 24.52 ± 1.97 |

## 5. Conclusions

A precipitation strengthened $(Fe_{0.3}Ni_{0.3}Mn_{0.3}Cr_{0.1})_{88}Ti_4Al_8$ HEA was fabricated by vacuum induction melting and casting, and the precipitation behavior during aging at 650 °C was investigated. The following conclusions are drawn:

1) The $L1_2$ precipitates showed a clear increase in size and decrease in number density during observed aging (2-244 hours), as determined by APT. There is likely an increase in number density associated with nucleation which occurs prior to 2 hours. The volume fraction fluctuates over time due to competition with B2. The APT results and LSW coarsening model show a transition from primarily nucleation and growth to primarily coarsening after aging for 24 hours, though both are present throughout the aging process. The growth kinetics deviated from other classical models due to interactions with the growing B2 phase, making the precipitation behavior complex.
2) The B2 and Chi phases did not form in amounts visible in SEM until 24 hours aging. Later, both phases grow to take up over half the structure at 120 hours. With longer aging times, the Chi phase begins to outgrow the B2 phase, although at 244 hours B2 still outnumbers Chi (25.75% vs 24.52%). In addition, early aging shows that Chi phase forms from Cr-enrichment around the B2 precipitates.
3) XRD analysis during in-situ aging verified the trends determined by APT and EBSD. Specifically, it shows a clear growth in size and volume fraction of $L1_2$ at early times, while B2 and Chi have just started nucleating. Later, after 24 hours of aging, the $L1_2$ volume fraction in the alloy decreases slightly while B2 coarsens and Chi grows during in-situ aging.
4) The cause of the increase of Chi at longer times and the interactions between B2 and $L1_2$ was rationalized based on the chemical potential of the elements in the alloy. Ni and Al show affinity to B2, causing B2 to be favored over $L1_2$. Thus, as B2 grows, $L1_2$ around it dissolves, causing the decrease in $L1_2$ volume fraction after 48 hours. Ti and Mn show affinity to Chi over B2, causing the Chi to grow at B2's expense. This re-introduces Ni into the matrix, allowing additional $L1_2$ to form.

**ACKNOWLEDGEMENTS**

This research was supported by the U.S. Nuclear Regulatory Commission Faculty Development Program (award number NRC 31310018M0044) and by U.S. National Science Foundation (award number DMR-2207965). Materials Research Center at Missouri University of Science and Technology is acknowledged for providing access to electron microscopes. Characterization using the JEM 2100F was performed at the Center for Nanoscale Materials at Argonne National Laboratory under user proposal 75825, with Dr. Yuzi Liu coordinating the effort. This research used resources of the Advanced Photon Source and the Center for Nanoscale Materials, U.S. Department of Energy (DOE) Office of Science User Facilities operated for the DOE Office of Science by Argonne National Laboratory under Contract No. DE-AC02-06CH11357. APT research was supported by the Center for Nanophase Materials Sciences (CNMS), which is a US Department of Energy, Office of Science User Facility at Oak Ridge National Laboratory. The authors would like to thank James Burns for assistance in performing APT sample preparation and running the APT experiments.

**References**

[1] Miracle, D.B., Senkov, O.N. (2017). A critical review of high entropy alloys and related concepts. *Acta Materialia, 122,* 448-511.

[2] Tsai, M.-H., Yeh, J.-W. (2014). High-Entropy Alloys: A Critical Review. *Materials Research Letters, 2*(3), 107-123.

[3] Cantor, B., Chang, I., Knight, P., & Vincent, A. (2004). Microstructural development in equiatomic multicomponent alloys. *Materials Science and Engineering: A*, *375-377*, 213–218.

[4] Yeh, J.-W., Chen, S.-K., Lin, S.-J., Gan, J.-Y., Chin, T.-S., Shun, T.-T., … Chang, S.-Y. (2004). Nanostructured High-Entropy Alloys with Multiple Principal Elements: Novel Alloy Design Concepts and Outcomes. *Advanced Engineering Materials*, *6*(5), 299–303.

[5] George, E.P., Curtin, W.A., Tasan, C.C. (2020). High entropy alloys: A focused review of mechanical properties and deformation mechanisms. *Acta Materialia, 188,* 435-474.

[6] Wang, X.F., Zhang, Y., Qiao, Y., Chen, G.L. (2007). Novel microstructure and properties of multicomponent $CoCrCuFeNiTi_x$ alloys. *Intermetallics, 15,* 357-362.

[7] Fu, Z., Chen, W., Wen, H., Zhang, D., Chen, Z., Zheng, B., Zhou, Y., Lavernia, E.J. (2016). Microstructure and strengthening mechanisms in an FCC structured single-phase nanocrystalline $Co_{25}Ni_{25}Fe_{25}Al_{7.5}Cu_{17.5}$ high-entropy alloy. *Acta Materialia, 107,* 59-71.

[8] Ma, Y., Hao, J., Jie, J., Wang, Q., Dong, C. (2019). Coherent precipitation and strengthening in a dual-phase $AlNi_2Co_2Fe_{1.5}Cr_{1.5}$ high-entropy alloy. *Materials Science and Engineering A, 764,* 138241.

[9] Bai, X., Fang, W., Chang, R., Yu, H., Zhang, X., Yin, F. (2019). Effects of Al and Ti additions on precipitation behavior and mechanical properties of $Co_{35}Cr_{25}Fe_{40-x}Ni_x$ TRIP high entropy alloys. *Materials Science and Engineering A, 767,* 138403.

[10] Chen, J., Zhou, X., Wang, W., Liu, B., Lu, Y., Yang, W., Xu, D., Liu, Y. (2018). A review on fundamentals of high entropy alloys with promising high-temperature properties. *Journal of Alloys and Compounds, 760,* 15-30.

[11] Liu, Y.Y, Chen, Z., Chen, Y.Z., Shi, J.C., Wang, Z.Y., Wang, S., Liu, F. (2019). Effect of Al content on high temperature oxidation of $Al_xCoCrCuFeNi$ high entropy alloys (x=0, 0.5, 1, 1.5, 2). *Vacuum, 169,* 108837.

[12] Li, T., Swanson, O.J., Frankel, G.S., Gerard, A.Y., Lu, P., Saal, J.E., Scully, J.R. (2019). Localized corrosion behavior of a single-phase non-equimolar high entropy alloy. *Electrochimica Acta, 306,* 71-84.

[13] Otto, F., Yang, Y., Bei, H., George, E.P. (2013). Relative effects of enthalpy and entropy on the phase stability of equiatomic high-entropy alloys. *Acta Materialia, 61,* 2628-2638.

[14] Steurer, W. (2020). Single-phase high-entropy alloys-A critical update. *Materials Characterization, 162,* 110179.

[15] Sonkusare, R., Jain, R., Biswas, K., Parameswaran, V., Gurao, N.P. (2020). High strain rate compression behaviour of single phase CoCuFeMnNi high entropy alloy. *Journal of Alloys and Compounds, 823,* 153763.

[16] Zhao, Y.L., Yang, T., Zhu, J.H., Chen, D., Yang, Y., Hu, A., Liu, C.T., Kai, J.-J. (2018). Development of high-strength Co-free high-entropy alloys hardened by nanosize precipitates. *Scripta Materialia*, *148*, 51-55.

[17] Yuan, J.L., Wu, Y.C., Liaw, P.K., Luan, J.H., Jiao, Z.B., Li, J., Han, P.D., Qiao, J.W. (2022). Remarkable cryogenic strengthening and toughening in nano-coherent $CoCrFeNiTi_{0.2}$ high-entropy alloys via energetically-tuning polymorphous precipitates. *Materials Science and Engineering A, 842,* 143111.

[18] Yang, T., Zhao, Y.L., Fan, L., Wei, J., Luan, J.H., Liu, W.H., Wang, C., Jiao, Z.B., Kai, J.J., Liu, C.T. (2020). Control of nanoscale precipitation and elimination of intermediate-temperature embrittlement in multicomponent high-entropy alloys. *Acta Materialia, 189,* 47-59.

[19] Gao, N., Lu, D.H., Zhao, Y.Y., Liu, G.H., Wu, Y., Liu, G., Fan, Z.T., Lu, Z.P., George, E.P. (2019). Strengthening of a CrMnFeCoNi high-entropy alloy by carbide precipitation. *Journal of Alloys and Compounds, 792,* 1028-1035.

[20] Dasari, S., Jagetia, A., Chang, Y.-J., Soni, V., Gwalani, B., Gorsse, S., Yeh, A.-C., Banerjee, R. (2020). Engineering multi-scale B2 precipitation in a heterogeeous FCC based microstructure to enhance the mechanical properties of a $Al_{0.5}Co_{1.5}CrFeNi_{1.5}$ high entropy alloy. *Journal of Alloys and Compounds, 830,* 154707.

[21] He, J.Y., Wang, H., Huang, H.L., Xu, X.D., Chen, M.W., Wu, Y., Liu, X.J., Nieh, T.G., An, K., Lu, Z.P. (2016) A precipitation-hardened high-entropy alloy with outstanding tensile properties. *Acta Materialia*, *102*, 187-196.

[22] Liang, Y.-J., Wang, L., Wen, Y., Cheng, B., Wu, Q., Cao, T., Xiao, Q., Xue, Y., Sha, G., Wang, Y., Ren, Y., Li, X., Wang, L., Wang, F., Cai, H. (2018). High-content ductile coherent nanoprecipitates achieve ultrastrong high-entropy alloys. *Nature Communications, 9*(1), 4063.

[23] Wang, L., Wang, L., Zhou, S., Xiao, Q., Xiao, Y., Wang, X., Cao, T., Ren, Y., Liang, Y.-J., Wang, L., Xue, Y. (2021). Precipitation and micromechanical behavior of the coherent ordered nanoprecipitation strengthened Al-Cr-Fe-Ni-V high entropy alloy. *Acta Materialia, 216*, 117121.

[24] Zhao, Y. Y., Chen, H. W., Lu, Z. P., Nieh, T. G. (2018). Thermal stability and coarsening of coherent particles in a precipitation-hardened (NiCoFeCr)94Ti2Al4 high-entropy alloy. *Acta Materialia*, *147*, 184–194.

[25] Lv, J., Fang, W., Bai, X., Yu, H., Xue, C., Zhang, X., Liu, B., Feng, J., Yin, F. (2023). Effect of Mo and V additions on the coarsening kinetics and high-temperature strength in γ′ precipitation-strengthened high-entropy alloys. *Materials Science and Engineering: A, 876*, 145145.

[26] He, J. Y., Wang, H., Wu, Y., Liu, X. J., Mao, H. H., Nieh, T. G., Lu, Z. P. (2016). Precipitation behavior and its effects on tensile properties of FeCoNiCr high-entropy alloys. *Intermetallics, 79*, 41–52.

[27] Deschamps, A., Hutchinson, C. R. (2021). Precipitation Kinetics in metallic alloys: Experiments and modeling. *Acta Materialia, 220,* 117338.

[28] Robson, J. D. (2004). Modelling the overlap of nucleation, growth and coarsening during precipitation. *Acta Materialia, 52*(15), 4669–4676.

[29] Zhao, Y., Chen, Z., Yan, K., Le, W., Naseem, S. (2021). Effects of aging treatment on the evolution of precipitated phase in CoCrFeNiTi0.6 high entropy alloys. *Journal of Alloys and Compounds, 887,* 161407.

[30] Ren, C., Sun, K., Jia, Y. F., Zhang, N. Z., Jia, Y. D., Wang, G. (2023). Effect of Mo addition on the microstructural evolution and mechanical properties of Fe–Ni–Cr–Mn–Al–Ti high entropy alloys. *Materials Science and Engineering: A, 864*, 144579.

[31] Laplanche, G., Berglund, S., Reinhart, C., Kostka, A., Fox, F., George, E. P. (2018). Phase stability and kinetics of σ-phase precipitation in CrMnFeCoNi high-entropy alloys. *Acta Materialia, 161*, 338–351.

[32] Laplanche, Guillaume. (2020). Growth kinetics of σ-phase precipitates and underlying diffusion processes in CrMnFeCoNi high-entropy alloys. *Acta Materialia, 199*, 193–208.

[33] Nandal, V., Sarvesha, R., Singh, S. S., Huang, E.-W., Chang, Y.-J., Yeh, A.-C., Neelakantan, S., Jain, J. (2021). Influence of pre-deformation on the precipitation characteristics of aged non-equiatomic Co1.5CrFeNi1.5 high entropy alloys with Ti and Al additions. *Journal of Alloys and Compounds, 855*, 157521.

[34] Wang, X., Zhang, Z., Wang, Z., Ren, X. (2022). Microstructural evolution and tensile properties of Al0.3CoCrFeNi high-entropy alloy associated with B2 precipitates. *Materials, 15*(3), 1215.

[35] Wu, X., Wang, B., Rehm, C., He, H., Naeem, M., Lan, S., Wu, Z., Wang, X.-L. (2022). Ultra-small-angle neutron scattering study on temperature-dependent precipitate evolution in CoCrFeNiMo0.3 high entropy alloy. *Acta Materialia, 222*, 117446.

[36] Fan, J., Fu, L., Sun, Y., Xu, F., Ding, Y., Wen, M., Shan, A. (2022). Unveiling the precipitation behavior and mechanical properties of co-free Ni47-xFe30Cr12Mn8AlxTi3 high-entropy alloys. *Journal of Materials Science & Technology, 118*, 25–34.

[37] Zhang, J. Y., Xiao, B., Li, Q., Cao, B. X., Hou, J. X., Liu, S. F., Zhang, J. X., Xiao, W. C., Luan, J. H., Zhao, Y. L., Liu, C. T., Yang, T. (2022). Temperature-dependent microstructural evolutions and deformation mechanisms of (Ni2Co2FeCr)92Al4Nb4 high-entropy alloys. *Journal of Alloys and Compounds, 918*, 165597.

[38] Li, Y., Zhou, J., Liu, Y., Lu, C., Shi, L., Zheng, W., Jin, W., Gao, Z., Yang, J., He, Y. (2023). Microstructural evolution and mechanical characterization for the AlCoCrFeNi2.1 eutectic high-entropy alloy under different temperatures. *Fatigue & Fracture of Engineering Materials & Structures, 46*(5), 1881–1892.

[39] Chen, D., He, F., Han, B., Wu, Q., Tong, Y., Zhao, Y., Wang, Z., Wang, J., Kai, J.-J. (2019). Synergistic effect of Ti and Al on L12-phase design in CoCrFeNi-based high entropy alloys. *Intermetallics*, *110*, 106476.

[40] Zhang, F., He, J., Wu, Y., Mao, H., Wang, H., Liu, X., Jiang, S., Nieh, T. G., Lu, Z. (2022). Effects of Ni and Al on precipitation behavior and mechanical properties of precipitation-hardened CoCrFeNi high-entropy alloys. *Materials Science and Engineering: A, 839*, 142879.

[41] Gwalani, B., Soni, V., Lee, M., Mantri, S., Ren, Y., Banerjee, R. (2017). Optimizing the coupled effects of Hall-Petch and precipitation strengthening in a Al0.3CoCrFeNi high entropy alloy. *Materials & Design, 121*, 254–260.

[42] Schneider, A., Inden, G. (2005). Simulation of the kinetics of precipitation reactions in ferritic steels. *Acta Materialia, 53*(2), 519–531.

[43] Lu, Y., Lu, G., Jia, D., Chen, Z. (2015). Phase-field study on competition precipitation process of Ni-Al-V Alloy. Transactions of Nonferrous Metals Society of China, 25(2), 544–551.

[44] Lin, C., Wu, W., Han, Y., Liu, J., Zhang, M., Wang, Q., Li, X. (2023). Orderly nucleation and competitive growth behaviors of Ti-Al intermetallic compounds in Ti/TiAl3 diffusion couple under high temperature. *Journal of Alloys and Compounds, 939*, 168815.

[45] Fang, J. Y. C., Liu, W. H., Luan, J. H., Yang, T., Wu, Y., Fu, M. W., Jiao, Z. B. (2022). Competition between continuous and discontinuous precipitation in L12-strengthened high-entropy alloys. *Intermetallics, 149*, 107655.

[46] Robson, J. D. (2013). Modeling competitive continuous and discontinuous precipitation. *Acta Materialia, 61*(20), 7781–7790.

[47] Deschamps, A., Brechet, Y. (1998). Influence of predeformation and ageing of an Al–Zn–Mg alloy—II. modeling of precipitation kinetics and yield stress. *Acta Materialia, 47*(1), 293–305.

[48] Hernandez-Santiago, F., Cayetano-Castro, N., Lopez-Hirata, V. M., Dorantes-Rosales, H. J., Cruz-Rivera, J. de. (2004). Precipitation Kinetics in a Cu-4 mass% Ti alloy. *Materials Transactions, 45*(7), 2312–2315.

[49] Luebbe, M., Duan, J., Zhang, F., Poplawsky, J., Pommeranke, H., Arivu, M., Hoffman, A., Buchely, M., & Wen, H. (2023). A high-strength precipitation hardened cobalt-free high-entropy alloy. *Materials Science and Engineering: A*, *870*, 144848.

[50] Thompson, K., Lawrence, D., Larson, D.J., Olson, J.D., Kelly, T.F., Gorman, B. (2007). In situ site-specific specimen preparation for atom probe tomography. *Ultramicroscopy*, *107*(2-3), 131-139.

[51] Ilavsky, J., Zhang, F., Andrews, R. N., Kuzmenko, I., Jemian, P. R., Levine, L. E., & Allen, A. J. (2018). Development of combined microstructure and structure characterization facility for *in situ* and *operando* studies at the Advanced Photon Source. *Journal of Applied Crystallography*, *51*(3), 867–882.

[52] Zhang, F., Levine, L. E., Allen, A. J., Young, S. W., Williams, M. E., Stoudt, M. R., Moon, K.-W., Heigel, J. C., & Ilavsky, J. (2019). Phase fraction and evolution of additively manufactured (AM) 15-5 stainless steel and Inconel 625 AM-bench artifacts. *Integrating Materials and Manufacturing Innovation*, *8*(3), 362–377. https://doi.org/10.1007/s40192-019-00148-1

[53] Lindwall, G., Campbell, C. E., Lass, E. A., Zhang, F., Stoudt, M. R., Allen, A. J., Levine, L. E. (2018). Simulation of TTT curves for additively manufactured Inconel 625. *Metallurgical and Materials Transactions A, 50*(1), 457–467.

[54] Lifshitz, I. M., & Slyozov, V. V. (1961). The kinetics of precipitation from Supersaturated Solid Solutions. *Journal of Physics and Chemistry of Solids*, *19*(1–2), 35–50. https://doi.org/10.1016/0022-3697(61)90054-3

[55] Li, Y., Wang, Z., Gao, X., Wang, Y., Li, J., & Wang, J. (2022b). Revisiting transient coarsening kinetics: A new framework in the Lifshitz-Slyozov-Wagner Space. *Acta Materialia*, *237*, 118196. https://doi.org/10.1016/j.actamat.2022.118196

[56] Liu, L., Zhang, Y., Wu, G., Yu, Y., Ma, Y., Ma, J., Baker, I., Zhang, Z. (2022). The effect of Al/Ti ratio on the evolution of precipitates and their effects on mechanical properties for Ni35(CoCrFe)55AlxTi10−x high entropy alloys. *Journal of Alloys and Compounds, 906*, 164291.